HHS Public Access

Author manuscript

Sci Transl Med. Author manuscript; available in PMC 2022 April 14.

Published in final edited form as:

Sci Transl Med. 2021 April 14; 13(589): . doi:10.1126/scitranslmed.abe9805.

Imaging *Enterobacterales* infections in patients using pathogen-specific positron emission tomography

Alvaro A. Ordonez[1,2,3,†], **Luz M. Wintaco**[4,5,†], **Filipa Mota**[1,2,3], **Andres F. Restrepo**[6], **Camilo A. Ruiz-Bedoya**[1,2,3], **Carlos F. Reyes**[7], **Luis G. Uribe**[8], **Sudhanshu Abhishek**[1,2,3], **Franco R. D'Alessio**[9], **Daniel P. Holt**[10], **Robert F. Dannals**[10], **Steven P. Rowe**[10], **Victor R. Castillo**[11], **Martin G. Pomper**[10], **Ulises Granados**[4,12,*], **Sanjay K. Jain**[1,2,3,10,*]

[1]Center for Infection and Inflammation Imaging Research, Johns Hopkins University School of Medicine, Baltimore, MD 21287, USA

[2]Center for Tuberculosis Research, Johns Hopkins University School of Medicine, Baltimore, MD 21287, USA

[3]Department of Pediatrics, Johns Hopkins University School of Medicine, Baltimore, MD 21287, USA

[4]Department of Nuclear Medicine, Hospital Internacional de Colombia, Fundación Cardiovascular de Colombia, Piedecuesta 681017, Colombia

[5]Biomedical and Biological Sciences Graduate Program, Escuela de Medicina y Ciencias de la Salud, Universidad del Rosario, Bogotá 111711, Colombia

[6]Department of Internal Medicine, Hospital Internacional de Colombia, Fundación Cardiovascular de Colombia, Piedecuesta 681017, Colombia

[7]Department of Critical Care, Hospital Internacional de Colombia, Fundación Cardiovascular de Colombia, Piedecuesta 681017, Colombia

[8]Department of Infectious Diseases, Hospital Internacional de Colombia, Fundación Cardiovascular de Colombia, Piedecuesta 681017, Colombia

[*]Corresponding author. ulisesgranados@fcv.org (U.G.); sjain5@jhmi.edu (S.K.J.).
[†]These authors contributed equally to this work.

Author contributions: A.A.O. and S.K.J. conceptualized and designed the study. A.A.O., L.M.W., A.F.R., C.F.R., L.G.U., F.R.D., S.P.R., and S.K.J. recruited patients and obtained consent. L.M.W., D.P.H., and R.F.D. synthesized ^{18}F-FDS. F.M. developed the solid-phase cartridge system to synthesize ^{18}F-FDS. A.A.O., L.M.W., and S.A. performed in vitro experiments. A.A.O., F.M., and C.A.R.-B. performed animal studies. S.P.R., M.G.P., and U.G. provided expertise on PET/CT imaging and image analysis. V.R.C. provided logistical support for patient imaging. A.A.O., L.M.W., U.G., and S.K.J. analyzed the data and performed statistical analysis. A.A.O. and S.K.J. wrote the initial draft, and all coauthors edited the manuscript. U.G. and S.K.J. provided funding and coordinated and supervised the project.

Competing interests: A.A.O. and S.K.J. are investigators on a research grant from T3 Pharmaceuticals AG, Switzerland and NovoBiotic Pharmaceuticals, Cambridge, MA, to Johns Hopkins University. A.A.O. received consulting fees from Cubresa Inc. A.A.O., M.G.P., and S.K.J. are co-inventors on pending patent US20150250906A1 on bacteria-specific labeled substrates as imaging biomarkers, filed by Johns Hopkins University. A.A.O., F.M., and S.K.J. are coinventors on pending patent USPA #63/071,755 on the solid-phase cartridge to formulate ready-to-use ^{18}F-FDS, filed by Johns Hopkins University.

Data and materials availability: All data associated with this study are present in the paper or the Supplementary Materials.

SUPPLEMENTARY MATERIALS

stm.sciencemag.org/cgi/content/full/13/589/eabe9805/DC1

[9]Pulmonary and Critical Care Medicine, Johns Hopkins University School of Medicine, Baltimore, MD 21287, USA

[10]Russell H. Morgan Department of Radiology and Radiological Sciences, Johns Hopkins University School of Medicine, Baltimore, MD 21287, USA

[11]Bioengineering Research Group, Fundación Cardiovascular de Colombia, Piedecuesta 681017, Colombia

[12]Biomedical and Translational Research Group, Fundación Cardiovascular de Colombia, Piedecuesta 681017, Colombia

Abstract

Enterobacterales represent the largest group of bacterial pathogens in humans and are responsible for severe, deep-seated infections, often resulting in sepsis or death. They are also a prominent cause of multidrug-resistant (MDR) infections, and some species are recognized as biothreat pathogens. Tools for noninvasive, whole-body analysis that can localize a pathogen with specificity are needed, but no such technology currently exists. We previously demonstrated that positron emission tomography (PET) with 2-deoxy-2-[^{18}F]fluoro-D-sorbitol (^{18}F-FDS) can selectively detect *Enterobacterales* infections in murine models. Here, we demonstrate that uptake of ^{18}F-FDS by bacteria occurs via a metabolically conserved sorbitol-specific pathway with rapid in vitro ^{18}F-FDS uptake noted in clinical strains, including MDR isolates. Whole-body ^{18}F-FDS PET/computerized tomography (CT) in 26 prospectively enrolled patients with either microbiologically confirmed *Enterobacterales* infection or other pathologies demonstrated that ^{18}F-FDS PET/CT was safe, could rapidly detect and localize *Enterobacterales* infections due to drug-susceptible or MDR strains, and differentiated them from sterile inflammation or cancerous lesions. Repeat imaging in the same patients monitored antibiotic efficacy with decreases in PET signal correlating with clinical improvement. To facilitate the use of ^{18}F-FDS, we developed a self-contained, solid-phase cartridge to rapidly (<10 min) formulate ready-to-use ^{18}F-FDS from commercially available 2-deoxy-2-[^{18}F]fluoro-D-glucose (^{18}F-FDG) at room temperature. In a hamster model, ^{18}F-FDS PET/CT also differentiated severe acute respiratory syndrome coronavirus 2 (SARS-CoV-2) pneumonia from secondary *Klebsiella pneumoniae* pneumonia—a leading cause of complications in hospitalized patients with COVID-19. These data support ^{18}F-FDS as an innovative and readily available, pathogen-specific PET technology with clinical applications.

INTRODUCTION

Enterobacterales are rod-shaped Gram-negative bacteria inhabiting the gastrointestinal tract, representing the largest group of bacterial pathogens in humans (1). They include *Escherichia coli, Klebsiella pneumoniae*, *Enterobacter* spp., *Salmonella* spp., *Serratia* spp., and *Yersinia* spp. (2), which produce a range of human disease including implant-associated infections, meningitis, brain abscesses, and nosocomial pneumonias that can result in sepsis or death. Multidrug-resistant (MDR) strains of *Enterobacterales* such as extended-spectrum β-lactamase (ESBL)–producing and carbapenem-resistant *Enterobacteriaceae* (CRE) are designated as urgent threats to human health by the U.S. Centers for Disease Control and

Prevention (3) and have become widespread globally. MDR infections due to *Enterobacterales* are associated with late diagnosis, a lower rate of appropriate empirical antibiotic treatment, and higher mortality (4). *Enterobacterales*, especially *K. pneumoniae*, are also a leading cause of secondary pneumonias in hospitalized patients with coronavirus disease 2019 (COVID-19) (5). Last, a prominent *Enterobacterales*, *Yersinia pestis* (causes plague), is designated as a biothreat pathogen and was responsible for several past pandemics (1).

Divergent evolution has created highly differentiated metabolic pathways between mammalian (eukaryotic) and bacterial (prokaryotic) cells (6), which can be exploited to develop bacteria-specific imaging approaches. 2-Deoxy-2-[^{18}F]fluoro-d-sorbitol (^{18}F-FDS) was identified by systematically screening random radiolabeled, small molecules for selective metabolism by bacteria (7). We have previously demonstrated that ^{18}F-FDS selectively accumulates in *Enterobacterales* but not in healthy mammalian or cancer cells and that ^{18}F-FDS positron emission tomography (PET) can specifically detect *Enterobacterales* infections in murine models (8). In this study, we prospectively assessed ^{18}F-FDS PET and computerized tomography (CT) in patients with microbiologically confirmed *Enterobacterales* infections before and after antibiotic treatment and compared them to control patients with other pathologies. We also developed a self-contained, solid-phase cartridge to rapidly synthesize ^{18}F-FDS and used it to evaluate *K. pneumoniae* coinfection in a hamster model of SARS-CoV-2.

RESULTS

Mechanism of incorporation of ^{18}F-FDS into bacteria

^{18}F-FDS uptake in *Enterobacterales* occurs via a metabolically conserved pathway mediated by a sorbitol-specific phosphotransferase system (PTS) composed of three subunits: SrlE, SrlA, and SrlB (9). The *srl* operon is induced by sorbitol, and PTS transports sorbitol with low micromolar affinities (10). *E. coli* K-12 *srlA*, *srlB*, and *srlE* knockout strains demonstrated that the sorbitol-specific PTS is essential for bacterial uptake of ^{18}F-FDS but not 2-deoxy-2-[^{18}F]fluoro-D-glucose (^{18}F-FDG) (fig. S1). However, no selective transporter for ^{18}F-FDS is present in mammalian cells, and substitution of the hydroxyl group by fluorine at the 2-position abrogates recognition by mammalian cells (11).

^{18}F-FDS PET/CT selectively detects *Enterobacterales* infection

In the current study, 26 newly identified patients with either microbiologically confirmed *Enterobacterales* infections (n = 18) or control patients with other pathologies (n = 8) were prospectively enrolled (Fig. 1 and table S1). For all infections, microbiological confirmation was required from the clinical/biopsy sample obtained from the infection site. Oncologic diagnoses were made via tissue biopsies, and sterile inflammatory pathologies were determined clinically and/or by tissue biopsies. Four patients with *Enterobacterales* infections had coexisting biopsy-proven oncologic disease. The median age was 60.5 years (range, 31 to 91 years), and 38% (10 of 26) were female (table S2). The cohort comprised a diverse group of patients with comorbidities and thus representative of hospitalized patients in a tertiary care setting. On the basis of the kinetics of radiotracer clearance (8, 12), ^{18}F-

FDS PET/CT was performed at 1 and 2 hours after an intravenous injection of ^{18}F-FDS. ^{18}F-FDS was rapidly eliminated predominantly via the kidneys with some hepatobiliary excretion and an overall low background PET signal (figs. S2 and S3). Overall, 71 ^{18}F-FDS PET/CT scans were performed in enrolled patients, which were safe, well tolerated, and without adverse effects in all patients.

^{18}F-FDS PET/CT was able to detect and localize infections at multiple body sites (Fig. 2, A and B). ^{18}F-FDS PET also detected an intracranial infection (Fig. 2C) over the inherently low ^{18}F-FDS background in the surrounding unaffected brain tissues (Fig. 2D and figs. S2 and S3). Consistent with previous reports (13, 14), acute infections were associated with a high bacterial burden at the infection sites (fig. S4A), and *Enterobacterales* isolated from the infected patients, including one ESBL-producing strain, demonstrated robust in vitro ^{18}F-FDS uptake (fig. S4B). There was no correlation between the peripheral white blood cell or neutrophil counts and the ^{18}F-FDS PET signal in the infected patients (fig. S5), suggesting that ^{18}F-FDS PET is not dependent on host inflammatory cells (8). Increased ^{18}F-FDS PET signal was observed at infection sites (Fig. 2E), whereas minimal signal was noted at the sites of oncologic or sterile inflammatory pathologies (Fig. 2F and fig. S2).

To quantify the PET signal, spherical volumes of interest (VOIs) were drawn at the sites of pathology and unaffected sites of the same tissue to calculate the target-to-nontarget tissue ratio (TNT). The ^{18}F-FDS PET signal 2 hours after injection was significantly higher ($P < 0.0001$) at the sites of *Enterobacterales* infection [TNT, 4.46; interquartile range (IQR), 3.32 to 4.95; Fig. 2G] than at the sites with oncologic/sterile inflammatory pathologies or infections due to non-*Enterobacterales* (TNT, 1.14; IQR, 0.98 to 1.50). Using a TNT cutoff of 3.0, ^{18}F-FDS PET at 2 hours after injection could identify infection sites with a sensitivity of 82% [95% confidence interval (CI), 55.8 to 95.3%] and a specificity of 100% (95% CI, 69.9% to 100%).

One patient (#5; table S2) with metastatic squamous cell carcinoma of the lung and *K. pneumoniae* pneumonia underwent ^{18}F-FDG PET/CT for clinical reasons 12 days after the study-related ^{18}F-FDS PET/CT (Fig. 3). Note the ^{18}F-FDG PET signal in the brain, which, as expected, is absent for ^{18}F-FDS PET. Whereas multiple pulmonary lesions were noted on CT and ^{18}F-FDG PET in this patient, several ^{18}F-FDG avid lesions (Fig. 3, red arrow) were not visualized on ^{18}F-FDS PET (Fig. 3, left panel).

^{18}F-FDS PET can monitor antibiotic treatments

Hospital-acquired infections due to MDR *Enterobacterales* have become widespread in the United States and globally (3). CRE infections are associated with late diagnosis, lower rate of appropriate empirical therapy, and considerably higher mortality rates (4). Bacterial metabolism of ^{18}F-FDS is mediated via highly conserved metabolic pathways with rapid and substantial in vitro ^{18}F-FDS uptake by clinical strains, including those that are MDR (ESBL or CRE) (fig. S4B) (7, 8). Thirteen patients with microbiologically confirmed *Enterobacterales* infections underwent repeat PET/CT after completion of antibiotic treatments (Fig. 4 and fig. S6). ^{18}F-FDS PET/CT from representative patients with successful or failed antibiotic treatment (due to the presence of MDR strain) is shown (Fig. 4, A and B). Overall, clinical improvement in patients (as determined independently by the

clinical team) was associated with a significant decrease (65%) in the lesion-specific ^{18}F-FDS PET activity with TNT of 4.70 (IQR, 3.92 to 5.21) and TNT of 1.64 (IQR, 1.21 to 2.83) before and after completion of antibiotic treatments, respectively (Fig. 4C; $P = 0.002$). However, lack of clinical improvement, e.g., treatment failure due to the presence of an MDR strain, did not lead to a decrease in ^{18}F-FDS PET activity (Fig. 4D). Monitoring of antibiotic treatments using ^{18}F-FDS PET could be a highly valuable clinical tool for the management of infected patients.

One-step synthesis and formulation of ^{18}F-FDS from ^{18}F-FDG

^{18}F-FDS can be synthesized rapidly from ^{18}F-FDG, which is widely available. However, current methods require the use of specialized equipment available in a radiochemistry laboratory (8, 15). Therefore, we developed a self-contained, one-step, solid-phase cartridge system to synthesize and formulate ready-to-use ^{18}F-FDS from commercially available ^{18}F-FDG in under 10 min at room temperature (Fig. 5). When starting with 857 ± 81 MBq of ^{18}F-FDG, this kit-based approach yielded 524 ± 68 MBq of ^{18}F-FDS with >90% radiochemical purity, which would be suitable for a typical ^{18}F-FDS dose required for an adult human (typically 370 MBq).

^{18}F-FDS can differentiate bacterial infection from SARS-CoV-2 pneumonitis in a hamster model

Enterobacterales, especially *K. pneumoniae*, are a leading cause of secondary pneumonia in hospitalized patients with COVID-19. We, therefore, tested whether ^{18}F-FDS PET could differentiate SARS-CoV-2 pneumonia from secondary *K. pneumoniae* pneumonia in a hamster model (Fig. 6A and fig. S7). Seven days after SARS-CoV-2 inoculation, the infectious viral load in the lungs was 2.20 ± 0.71 $\log_{10}$ 50% tissue culture infective dose ($TCID_{50}$) per milliliter, and CT demonstrated a robust pneumonia with corresponding pulmonary ^{18}F-FDG PET signal (Fig. 6B). However, as anticipated, no pulmonary ^{18}F-FDS PET was noted with SARS-CoV-2 pneumonia (Fig. 6C and movie S1). PET was repeated in the same animals after establishing a secondary pneumonia with *K. pneumoniae* (Fig. 6D and movie S2). ^{18}F-FDS PET demonstrated a robust signal in the lungs (Fig. 6E; TNT, 7.39; IQR, 6.47 to 10.34), which was significantly higher than the pulmonary signal noted with SARS-CoV-2 pneumonia before the secondary bacterial pneumonia (TNT, 1.39; IQR, 1.25 to 1.52; $P = 0.002$). At the time of imaging, the bacterial burden was 10.45 ± 0.35 $\log_{10}$ colony-forming units (CFU) per milliliter, and the viral burden was 1.12 ± 0.09 $\log_{10}$ $TCID_{50}$ per milliliter.

DISCUSSION

When infections occur in an inaccessible site, clinical samples (blood, urine, stool, or cerebrospinal fluid) can often yield nondiagnostic results or are otherwise insensitive for deep-seated infections. For example, a systematic review demonstrated that blood cultures for patients hospitalized with pneumonia were true positives in 0 to 14% of patients (16). Invasive procedures (e.g., bronchoalveolar lavage) or surgical resection/biopsy is often used for establishing a definitive diagnosis. However, the time and effort required for invasive procedures can delay diagnosis, may be dangerous, and are generally limited to the most

accessible lesion, identified at a single time point. Therefore, noninvasive tools such as CT, magnetic resonance imaging (MRI), or nuclear medicine techniques such as radiolabeled white blood cell imaging and ^{18}F-FDG PET are often incorporated into the diagnostic workup of such patients. However, those imaging tools detect morphologic changes or host immune responses to infection and thereby cannot reliably differentiate oncologic, inflammatory, or infectious pathologies (17). Moreover, host responses to infection may be reduced or absent in immunosuppressed patients (e.g., cancer chemotherapy, HIV/AIDS, and organ transplant), who are also most at risk for infection. Last, current approaches fail to provide rapid feedback about the effect, or adequacy, of a selected antibiotic regimen. Therefore, there is a need for rapid, whole-body imaging that could localize a pathogen with specificity and provide a quantitative readout of disease burden. However, thus far, no such technology is available clinically (17).

In this prospective study, ^{18}F-FDS PET/CT detected and localized infections at multiple body sites. Pneumonia was noted in several patients in the study, which is consistent with the observation that *Enterobacterales* account for 30% of healthcare-associated pneumonias (18) and up to 55% of all ventilator-associated pneumonias (VAPs) (19, 20), with an associated mortality of 24 to 50% (21). Osteoarticular/soft tissue infections were also well visualized, especially due to low background in healthy bone and muscle tissues. *Enterobacterales* are an important cause of lower extremity infections (22). In addition, *Salmonella* spp. are the leading cause of osteoarticular infections in patients with sickle hemoglobinopathies (23, 24), which are challenging to diagnose because their clinical and imaging findings are similar to those of bone infarcts, which also occur frequently in these patients (25). *Salmonella* readily takes up ^{18}F-FDS and, therefore, ^{18}F-FDS PET may be useful for the diagnosis of infections in patients with sickle hemo globinopathies (8). ^{18}F-FDS is rapidly cleared from circulation and primarily excreted through the urinary system, with small amounts also excreted through the hepatobiliary system. Subse-quent ^{18}F-FDS PET signal is noted in the gastrointestinal system within 2 hours in mice and after 150 min in humans, a late time point that was not captured in the current study (8, 12). ^{18}F-FDS PET is still useful to diagnose abdominal infections. Spatial information provided by co-registering the PET with anatomical imaging (CT and MRI) can differentiate the intraluminal signal due to normal flora versus extraluminal signal representing an infection (e.g., peritonitis and abscess). As anticipated, only minimal signal was noted at the sites of oncologic or sterile inflammatory pathologies. Kang *et al.* (26) have recently demonstrated in mice that ^{18}F-FDS PET signal was significantly higher in tumors colonized by live *E. coli* than those without infection, and ^{18}F-FDS PET signal strongly correlated with the bacterial burden in tumors, supporting our observation demonstrating minimal ^{18}F-FDS uptake in cancerous lesions compared to that of tissues infected with *Enterobacterales*.

PET has become a routine clinical tool, particularly for oncology, neurology, and cardiology (27), and is increasingly available in both developed and developing countries (28). PET typically takes 15 to 60 min (depending on body coverage), performed 1 to 2 hours after an intravenous administration of the tracer. New developments such as the total-body PET scanner will shorten the scan duration while increasing sensitivity (29). Because of the short half-life of most PET radionuclides, e.g., 109 min for F-18, the tracer has to be synthesized either on-site or at a nearby location, which requires the availability of dedicated

infrastructure (cyclotron) and trained personnel, thus limiting on-demand supply. A major advantage of ^{18}F-FDS is the ability to synthesize it rapidly from ^{18}F-FDG, which is widely available. In addition, high specific activity (radioactivity per mass) is not required because even low specific activity ^{18}F-FDS (20 to 50 Ci/mM) produces optimal imaging characteristics (7, 8). Therefore, we developed a self-contained, solid-phase cartridge system to synthesize and formulate ready-to-use ^{18}F-FDS from commercially available ^{18}F-FDG in under 10 min at room temperature with minimal equipment requirements. We believe this to be a major advantage of this technology as it could be synthesized on-demand at essentially any site with access to ^{18}F-FDG.

Although COVID-19 in humans is frequently a mild illness, some patients develop acute respiratory distress syndrome (ARDS) requiring mechanical ventilation (30). Prolonged ventilatory support, presence of comorbidities, and the increased use of immunomodulatory medications lead to an increased risk of bacterial pneumonia in this population (31, 32). In patients with severe COVID-19, an accurate and timely diagnosis is required to identify, or exclude, bacterial pathogens, which may present initially as coinfections or arise later in the course of the disease. Bronchoalveolar lavage samples have traditionally been used to isolate the causative pathogen and determine antibiotic therapy. However, some institutions have placed limitations on bronchoscopic procedures for patients with COVID-19 due to the risk of viral aerosolization (33). Chest radiographs and CT are also routinely used in the evaluation of VAP, but in some cases, they can be difficult to interpret because they rely on the presence of nonspecific structural abnormalities that can mimic other pathologies, including COVID-19 (34). Given that *Enterobacterales* are the leading pathogens causing VAP in hospitalized patients with COVID-19 (5), we evaluated ^{18}F-FDS PET/CT in a hamster model of SARS-CoV-2 and *K. pneumoniae* coinfection. ^{18}F-FDS PET/CT was able to noninvasively differentiate bacterial from viral pneumonia and determine the extent of the disease, with significantly higher TNT in the bacterial coinfection compared to viral pneumonia. These data support the specificity of ^{18}F-FDS PET/CT and its utility to detect secondary pneumonia due to *Enterobacterales* infections.

Our study has several limitations. A large hepatic abscess was not adequately visualized by ^{18}F-FDS PET, demonstrating a focus of photopenia (fig. S8A), likely due to limited ^{18}F-FDS access into large avascular lesions. Central photopenia with large abscesses has also been noted with ^{18}F-FDG PET, which is generally considered highly sensitive (35). In addition, when using a TNT cutoff of 3.0, sites of *Enterobacterales* infection in two patients with diabetes were below this threshold (fig. S8, B and C). Patients with diabetes have impaired venous drainage, which could have contributed to an increase in the background signal and thus a lack of a sufficiently high TNT. ^{18}F-FDS PET signal was also noted in likely uninfected fluids, g., large joints and pleural and peritoneal effusions (fig. S9), which needs to be assessed in future studies. PET uptake in pleural fluids may also be noted with ^{18}F-FDG (36), and the underlying basis for these findings needs to be better understood. Although the stringent criteria used in this study—prospective enrollment, microbiological confirmation required from the clinical/biopsy sample obtained from the infection site, and inclusion of patients who received ≤72 hours of antibiotic treatment by the time of first ^{18}F-FDS PET—are a major strength (17), they were also an impediment to patient recruitment. However, the patient cohort was representative of hospitalized patients in a tertiary care

setting, and a validated PET tracer in clinical use would not be subject to such restrictions. Moreover, due to the ease of tracer synthesis, this technology could be implemented practically, especially with on-demand, one-step, solid-phase cartridge system synthesis, becoming a valuable adjunct to traditional approaches used for infectious diseases. Some brain tumors or inflammatory pathologies may accumulate ^{18}F-FDS (37, 38); however, these reports describe pituitary lesions, which are anatomically outside the blood-brain barrier, and thus have a higher background signal compared to the brain parenchyma. Moreover, some measurements were made at 5 min after tracer injection in the context of low signal with high background versus 60 and 120 min after tracer injection in our current study due to the time needed for clearance of the background signal (8, 12). Therefore, the findings noted in pituitary lesions are likely consistent with a nonspecific blood pool effect, that is, capillary leak at the site of inflammation or tumor (39). Last, although this study demonstrates proof of concept and feasibility of bacteria-specific tracers in patients, the sample size is relatively small. Therefore, larger studies are needed to validate these findings.

In summary, we present data from a prospective clinical study evaluating whole-body ^{18}F-FDS PET/CT in newly identified, microbiologically confirmed *Enterobacterales* infections. We demonstrate that ^{18}F-FDS PET is safe, can rapidly and specifically detect and differentiate *Enterobacterales* infections from other pathologies, and can monitor antibiotic efficacy with clinical improvement associated with decreases in PET signal. ^{18}F-FDS uptake in bacteria is mediated via highly conserved metabolic pathways with the ability to detect both drug-sensitive and MDR infection in situ. Although larger clinical studies are needed to validate these findings, our data support the role of ^{18}F-FDS as an easily synthesizable, bacteria class–specific PET tracer with clinical applications.

MATERIALS AND METHODS

Study design

The objective of this study was to assess ^{18}F-FDS PET in patients with infections due to *Enterobacterales* and those with inflammatory and/or oncologic disease. No sample size calculations were performed. The investigators involved in this study were not blinded during data collection and/or analysis. Determination of whether a patient had clinical improvement after completion of antibiotic treatments was assessed independently by the clinical team, and the study team was blinded to these results. The study team had no role in the diagnosis or clinical management of the patients. Thirty-seven eligible patients (table S1) with microbiologically confirmed or high suspicion for *Enterobacterales* infection and control patients with other pathologies were prospectively enrolled between November 2016 and May 2020 at the Fundación Cardiovascular de Colombia–Hospital Internacional de Colombia (HIC) or the Johns Hopkins Hospitals (JHH) (table S2). Written informed consent was obtained from all patients, and de-identified PET/CT images are presented. Six consented patients were excluded: one patient due to motion artifact during the scan, two patients because the tracer could not be administered, and three patients because surgical procedures (debridement/drainage) were performed before the scan. An additional five enrolled patients were excluded because a definite microbiological (or other) diagnosis

could not be established per our preestablished criteria. These studies were approved by the Hospital Internacional de Colombia (acta #459) and Johns Hopkins University Institutional Review Board Committee (IRB00097331). ^{18}F-FDS was used per the Good Manufacturing Practices for Manufacturing Radiopharmaceuticals, Ministerio de Salud y Protección Social, Colombia (40), or the U.S. Food and Drug Administration Radioactive Drug Research Committee program guidelines for investigational drugs (41). There was no external data and safety monitoring board. All protocols were approved by the Johns Hopkins University Biosafety, Radiation Safety, Animal Care and Use and Institutional Review Board Committees, and the Hospital Internacional de Colombia Institutional Review Board and Scientific Committees.

Imaging

^{18}F-FDS was synthesized at the Johns Hopkins PET Radiotracer Center using current good manufacturing practices or at the HIC radiopharmacy per local regulations. A slow intravenous push of 370.4 ± 47.2 MBq of ^{18}F-FDS was administered to study participants, and ^{18}F-FDS-PET/CT was acquired at 60 and 120 min after tracer injection. At JHH, a Siemens Biograph mCT 128-slice scanner was used and PET images were obtained from the skull vertex to mid-thigh with 3 min per bed position. At HIC, a General Electric Discovery IQ 600 scanner was used with the same acquisition parameters. Noncontrast CT scans were used for attenuation correction and localization. CT parameters included 120 kVp, 80 mAs, 4-mm slice thickness, and 3.3-mm slice increment.

Bacterial strains and assays

Reference bacterial strains purchased from the American Type Culture Collection [*E. coli* (ATCC 25922)] or Horizon Discovery [*E. coli* K-12 (parent strain, BW25113) and *E. coli* K-12 *srlA*, *srlB*, and *srlE* knockout strains (Keio Knockout Collection) (42)] and clinical strains from the clinical microbiology laboratory (HIC) were aerobically grown to an absorbance at 600 nm of 1.0 in lysogeny broth (LB). The number of CFU was enumerated by dilution and plated onto solidified LB medium. In vitro uptake of ^{18}F-FDS assays was performed as described before with 20 kBq/ml at 37°C with rapid agitation (8).

Solid-phase cartridge system to synthesize ^{18}F-FDS

Unless specified otherwise, all other reagents and materials were purchased from Sigma-Aldrich. A synthesis cartridge was prepared by packing a solid-phase extraction tube (2 ml) with 500 mg of macroporous triethylammonium methylpolystyrene borohydride (Biotage) between two frits (20-μm porosity). ^{18}F-FDG (857 ± 81 MBq; Sofie Co.) was passed through a synthesis cartridge and Chromabond Set V cartridge (ABX), in tandem, over 5 min. The syringes were flushed with saline (20 ml, discarding the first 10 ml). ^{18}F-FDS (524 ± 68 MBq, pH 6, 61 ± 2% non–decay-corrected radiochemical yield) was eluted into a sterile vial in 97 ± 2% radiochemical purity assessed by radio-TLC (thin-layer chromatography) (AR-2000, Eckert & Ziegler).

Animal studies

Syrian golden hamsters (male, 6 to 7 weeks old; Envigo) were used. SARS-CoV-2/USA-WA1/2020 strain (BEI Resources, National Institute of Allergy and Infectious Diseases) was propagated with one passage in cell cultures in a biosafety level-3 (BSL-3) laboratory (JHH). Animals were challenged with 1.5×10^5 $TCID_{50}$ in 100 μl by intranasal route (43). The pneumonia model, adapted from Weinstein *et al.* (8), was established by intratracheal installation of *K. pneumoniae* (ATCC 43816) (3 $\log_{10}$ CFU). Live animals were imaged inside in-house developed, sealed biocontainment devices compliant with BSL-3 (44, 45). Seven days after infection, SARS-CoV-2–infected hamsters underwent PET using ^{18}F-FDG (7.13 ± 0.91 MBq, $n = 8$) and ^{18}F-FDS (cartridge-synthesized, 7.58 ± 0.59 MBq, $n = 6$) administered intravenously via the penile vein. A 15-min PET acquisition was performed using the nanoScan PET/CT (Mediso) 45 min (^{18}F-FDG) or 120 min (^{18}F-FDS) after tracer injection (8). PET images were acquired within one field of view. Noncontrast CT was subsequently acquired for anatomical co-registration. CT acquisition parameters included 480 projections, 50-kVp tube voltage, 600 μA, 300-ms exposure time, 1:4 binning, and helical acquisition. Animals were infected with *K. pneumoniae* after imaging, and repeat ^{18}F-FDS PET (7.14 ± 2.32 MBq, $n = 6$) was performed 36 hours after the bacterial infection. No animal was excluded from the analyses.

Image analysis

Human PET data were visualized using OsiriX MD 11.0 DICOM Viewer (Pixmeo SARL). VivoQuant 2020 (Invicro) was used for animal data. VOIs were manually drawn using CT as a guide and applied to the PET dataset (44, 46).

Statistical analysis

Prism 8.2 (GraphPad Software Inc.) was used for the data analysis. CFU data ($\log_{10}$ scale) and in vitro uptake of ^{18}F-FDS are presented as mean and SD. PET data presented as median and IQR were compared using a Mann-Whitney *U* test. Correlation analysis was performed using Pearson analysis. *P* values <0.05 were considered statistically significant. Individual subject-level data are reported in data file S1.

Supplementary Material

Refer to Web version on PubMed Central for supplementary material.

Acknowledgments:

We thank all the patients who participated in the study. In addition, we want to thank the Nuclear Medicine, Internal Medicine, and Microbiology teams at Johns Hopkins Hospitals (JHH) and Hospital Internacional de Colombia (HIC) for supporting the human imaging studies. We also thank M. Lopez, D. C. Lesmes, and N. C. Serrano for their support with the clinical studies at HIC; K. Flavahan and P. De Jesus (JHH) for supporting the animal studies; C. K. Bullen (JHH) for viral studies; and H. T. Ravert (JHH) for assisting with radiochemical syntheses.

Funding: This work was funded by the U.S. NIH (R01-HL131829, R01-AI153349, and Director's Transformative Research Award R01-EB020539), Department of Defense's Congressionally Directed Medical Research Programs PR-171338P1, Maryland Innovation Initiative to S.K.J., and Colciencias 656677758411 #832-2017 to U.G. Animal studies were supported by the Center for Infection and Inflammation Imaging Research (Johns Hopkins University). Support from P41EB024495 is also acknowledged.

REFERENCES AND NOTES

1. Donnenberg MS, Mandell, Douglas, and Bennett's Principles and Practice of Infectious Diseases, Gerald JEB Mandell L, Dolin R, Eds. (Elsevier Inc., 2010), chap. 218, pp. 2815–2833.
2. Guentzel MN, in Medical Microbiology, Baron S, Ed. (University of Texas Medical Branch at Galveston, 1996), chap. 26.
3. Centers for Disease Control and Prevention, Antibiotic Resistance Threats in the United States (Centers for Disease Control and Prevention, 2019); https://cdc.gov/drugresistance/pdf/threats-report/2019-ar-threats-report-508.pdf.
4. Sabino S, Soares S, Ramos F, Moretti M, Zavascki AP, Rigatto MH, A cohort study of the impact of carbapenem-resistant Enterobacteriaceae infections on mortality of patients presenting with sepsis. mSphere 4, e00052–19 (2019).
5. Dhesi Z, Enne VI, Brealey D, Livermore DM, High J, Russell C, Colles A, Kandil H, Mack D, Martin D, Page V, Parker R, Roulston K, Singh S, Wey E, Swart AM, Stirling S, Barber JA, O'Grady J, Gant VA, Organisms causing secondary pneumonias in COVID-19 patients at 5 UK ICUs as detected with the FilmArray test. medRxiv 10.1101/2020.2006.2022.20131573, (2020).
6. Mac Faddin JF, Biochemical Tests for Identification of Medical Bacteria (Williams & Wilkins, 1976).
7. Ordonez AA, Weinstein EA, Bambarger LE, Saini V, Chang YS, DeMarco VP, Klunk MH, Urbanowski ME, Moulton KL, Murawski AM, Pokkali S, Kalinda AS, Jain SK, A systematic approach for developing bacteria-specific imaging tracers. J. Nucl. Med 58, 144–150 (2017). [PubMed: 27635025]
8. Weinstein EA, Ordonez AA, DeMarco VP, Murawski AM, Pokkali S, MacDonald EM, Klunk M, Mease RC, Pomper MG, Jain SK, Imaging Enterobacteriaceae infection in vivo with ^{18}F-fluorodeoxysorbitol positron emission tomography. Sci. Transl. Med 6, 259ra146 (2014).
9. Yamada M, Saier MH Jr., Physical and genetic characterization of the glucitol operon in Escherichia coli. J. Bacteriol 169, 2990–2994 (1987). [PubMed: 3036766]
10. Lengeler J, Mutations affecting transport of the hexitols D-mannitol, D-glucitol, and galactitol in Escherichia coli K-12: Isolation and mapping. J. Bacteriol 124, 26–38 (1975). [PubMed: 1100602]
11. Scott ME, Viola RE, The use of fluoro- and deoxy-substrate analogs to examine binding specificity and catalysis in the enzymes of the sorbitol pathway. Carbohydr. Res 313, 247–253 (1998). [PubMed: 10209867]
12. Zhu W, Yao S, Xing H, Zhang H, Tai YC, Zhang Y, Liu Y, Ma Y, Wu C, Wang H, Li Z, Wu Z, Zhu Z, Li F, Huo L, Biodistribution and radiation dosimetry of the Enterobacteriaceae-specific imaging probe [^{18}F]Fluorodeoxysorbitol determined by PET/CT in healthy human volunteers. Mol. Imaging Biol 18, 782–787 (2016). [PubMed: 27020679]
13. König C, Simmen HP, Blaser J, Bacterial concentrations in pus and infected peritoneal fluid—Implications for bactericidal activity of antibiotics. J. Antimicrob. Chemother 42, 227–232 (1998). [PubMed: 9738841]
14. American Thoracic Society; Infectious Diseases Society of America, Guidelines for the management of adults with hospital-acquired, ventilator-associated, and healthcare-associated pneumonia. Am. J. Respir. Crit. Care Med 171, 388–416 (2005). [PubMed: 15699079]
15. Li ZB, Wu Z, Cao Q, Dick DW, Tseng JR, Gambhir SS, Chen X, The synthesis of ^{18}F-FDS and its potential application in molecular imaging. Mol. Imaging Biol 10, 92–98 (2008). [PubMed: 18097725]
16. Afshar N, Tabas J, Afshar K, Silbergleit R, Blood cultures for community-acquired pneumonia: Are they worthy of two quality measures? A systematic review. J. Hosp. Med 4, 112–123 (2009). [PubMed: 19219920]
17. Ordonez AA, Sellmyer MA, Gowrishankar G, Ruiz-Bedoya CA, Tucker EW, Palestro CJ, Hammoud DA, Jain SK, Molecular imaging of bacterial infections: Overcoming the barriers to clinical translation. Sci. Transl. Med 11, eaax8251 (2019).
18. Magill SS, O'Leary E, Janelle SJ, Thompson DL, Dumyati G, Nadle J, Wilson LE, Kainer MA, Lynfield R, Greissman S, Ray SM, Beldavs Z, Gross C, Bamberg W, Sievers M, Concannon C, Buhr N, Warnke L, Maloney M, Ocampo V, Brooks J, Oyewumi T, Sharmin S, Richards K,

Rainbow J, Samper M, Hancock EB, Leaptrot D, Scalise E, Badrun F, Phelps R, Edwards JR; Emerging Infections Program Hospital Prevalence Survey Team, Changes in prevalence of health care–associated infections in U.S. hospitals. N. Engl. J. Med 379, 1732–1744 (2018). [PubMed: 30380384]

19. Rhodes NJ, Cruce CE, O'Donnell JN, Wunderink RG, Hauser AR, Resistance trends and treatment options in gram-negative ventilator-associated pneumonia. Curr. Infect. Dis. Rep 20, 3 (2018). [PubMed: 29511909]
20. Sader HS, Castanheira M, Flamm RK, Antimicrobial activity of ceftazidime-avibactam against Gram-negative bacteria isolated from patients hospitalized with pneumonia in US medical centers, 2011 to 2015. Antimicrob. Agents Chemother 61, e02083–16 (2017).
21. Chastre J, Fagon J-Y, Ventilator-associated pneumonia. Am. J. Respir. Crit. Care Med 165, 867–903 (2002). [PubMed: 11934711]
22. Ki V, Rotstein C, Bacterial skin and soft tissue infections in adults: A review of their epidemiology, pathogenesis, diagnosis, treatment and site of care. Can. J. Infect. Dis. Med. Microbiol 19, 173–184 (2008).
23. Kaplan J, Ikeda S, McNeil JC, Kaplan SL, Vallejo JG, Microbiology of osteoarticular infections in patients with sickle hemoglobinopathies at Texas Children's Hospital, 2000–2018. Pediatr. Infect. Dis. J 38, 1251–1253 (2019). [PubMed: 31738345]
24. Tordjman D, Holvoet L, Benkerrou M, Ilharreborde B, Mazda K, Pennecot GF, Fitoussi F, Hematogenous osteoarticular infections of the hand and the wrist in children with sickle cell anemia: Preliminary report. J. Pediatr. Orthop 34, 123–128 (2014). [PubMed: 23812139]
25. Vanderhave KL, Perkins CA, Scannell B, Brighton BK, Orthopaedic manifestations of sickle cell disease. J. Am. Acad. Orthop. Surg 26, 94–101 (2018). [PubMed: 29309293]
26. Kang SR, Jo EJ, Nguyen VH, Zhang Y, Yoon HS, Pyo A, Kim DY, Hong Y, Bom HS, Min JJ, Imaging of tumor colonization by Escherichia coliusing ^{18}F-FDS PET. Theranostics 10, 4958–4966 (2020). [PubMed: 32308761]
27. James ML, Gambhir SS, A molecular imaging primer: Modalities, imaging agents, and applications. Physiol. Rev 92, 897–965 (2012). [PubMed: 22535898]
28. Jain SK, The promise of molecular imaging in the study and treatment of infectious diseases. Mol. Imaging Biol 19, 341–347 (2017). [PubMed: 28155078]
29. Cherry SR, Badawi RD, Karp JS, Moses WW, Price P, Jones T, Total-body imaging: Transforming the role of positron emission tomography. Sci. Transl. Med 9, eaaf6169 (2017).
30. Richardson S, Hirsch JS, Narasimhan M, Crawford JM, McGinn T, Davidson KW; the Northwell COVID-19 Research Consortium, Barnaby DP, Becker LB, Chelico JD, Cohen SL, Cookingham J, Coppa K, Diefenbach MA, Dominello AJ, Duer-Hefele J, Falzon L, Gitlin J, Hajizadeh N, Harvin TG, Hirschwerk DA, Kim EJ, Kozel ZM, Marrast LM, Mogavero JN, Osorio GA, Qiu M, Zanos TP, Presenting characteristics, comorbidities, and outcomes among 5700 patients hospitalized with COVID-19 in the New York city area. JAMA 323, 2052–2059 (2020). [PubMed: 32320003]
31. Zhou F, Yu T, Du R, Fan G, Liu Y, Liu Z, Xiang J, Wang Y, Song B, Gu X, Guan L, Wei Y, Li H, Wu X, Xu J, Tu S, Zhang Y, Chen H, Cao B, Clinical course and risk factors for mortality of adult inpatients with COVID-19 in Wuhan, China: A retrospective cohort study. Lancet 395, 1054–1062 (2020). [PubMed: 32171076]
32. Grasselli G, Zangrillo A, Zanella A, Antonelli M, Cabrini L, Castelli A, Cereda D, Coluccello A, Foti G, Fumagalli R, Iotti G, Latronico N, Lorini L, Merler S, Natalini G, Piatti A, Ranieri MV, Scandroglio AM, Storti E, Cecconi M, Pesenti A; COVID-19 Lombardy ICU Network, Baseline characteristics and outcomes of 1591 patients infected with SARS-CoV-2 admitted to ICUs of the Lombardy Region, Italy. JAMA 323, 1574–1581 (2020). [PubMed: 32250385]
33. Wahidi MM, Shojaee S, Lamb CR, Ost D, Maldonado F, Eapen G, Caroff DA, Stevens MP, Ouellette DR, Lilly C, Gardner DD, Glisinski K, Pennington K, Alalawi R, The use of bronchoscopy during the Coronavirus Disease 2019 pandemic: CHEST/AABIP guideline and expert panel report. Chest 158, 1268–1281 (2020). [PubMed: 32361152]
34. Wunderink RG, Radiologic diagnosis of ventilator-associated pneumonia. Chest 117, 188S–190S (2000). [PubMed: 10816034]

35. Xia Q, Feng Y, Wu C, Huang G, Liu J, Chen T, Sun X, Song S, Tong L, Ni Y, Differentiation between malignant and benign solitary lesions in the liver with ^{18}FDG PET/CT: Accuracy of age-related diagnostic standard. J. Cancer 6, 40–47 (2015). [PubMed: 25553087]
36. Porcel JM, Hernandez P, Martinez-Alonso M, Bielsa S, Salud A, Accuracy of fluorodeoxyglucose-PET imaging for differentiating benign from malignant pleural effusions: A meta-analysis. Chest 147, 502–512 (2015). [PubMed: 25188411]
37. Kong Z, Wang Y, Ma W, Cheng X, Role of ^{18}F-fluorodeoxyglucose (FDG) and ^{18}F-2-fluorodeoxy sorbitol (FDS) in autoimmune hypophysitis: A case report. BMC Endocr. Disord 20, 84 (2020). [PubMed: 32517690]
38. Cheng X, Zhu W, Cui R, Increased ^{18}F-2-Fluorodeoxysorbitol (^{18}F-FDS) activity in a pituitary spindle cell carcinoma. Clin. Nucl. Med 41, 953–955 (2016). [PubMed: 27764039]
39. Javadi MS, Ordonez AA, Jain SK, Re: Increased ^{18}F-2-Fluorodeoxysorbitol (^{18}F-FDS) activity in a pituitary spindle cell carcinoma. Clin. Nucl. Med 42, 649 (2017).
40. Ministerio de Salud y Protección Social, Republica de Colombia. Resolución 4245 de 2015; https://minsalud.gov.co/Normatividad_Nuevo/Resoluci%C3%B3n%204245%20de%202015.pdf.
41. U.S. Food and Drug Administration, Guidance for Industry and Researchers: The Radioactive Drug Research Committee: Human Research Without an Investigational New Drug Application (U.S. Food and Drug Administration, 2010); http://fda.gov/downloads/Drugs/Guidances/UCM163892.pdf.
42. Baba T, Ara T, Hasegawa M, Takai Y, Okumura Y, Baba M, Datsenko KA, Tomita M, Wanner BL, Mori H, Construction of Escherichia coli K-12 in-frame, single-gene knockout mutants: The Keio collection. Mol. Syst. Biol 2, 2006.0008 (2006).
43. Imai M, Iwatsuki-Horimoto K, Hatta M, Loeber S, Halfmann PJ, Nakajima N, Watanabe T, Ujie M, Takahashi K, Ito M, Yamada S, Fan S, Chiba S, Kuroda M, Guan L, Takada K, Armbrust T, Balogh A, Furusawa Y, Okuda M, Ueki H, Yasuhara A, Sakai-Tagawa Y, Lopes TJS, Kiso M, Yamayoshi S, Kinoshita N, Ohmagari N, Hattori SI, Takeda M, Mitsuya H, Krammer F, Suzuki T, Kawaoka Y, Syrian hamsters as a small animal model for SARS-CoV-2 infection and countermeasure development. Proc. Natl. Acad. Sci. U.S.A 117, 16587–16595 (2020). [PubMed: 32571934]
44. Tucker EW, Guglieri-Lopez B, Ordonez AA, Ritchie B, Klunk MH, Sharma R, Chang YS, Sanchez-Bautista J, Frey S, Lodge MA, Rowe SP, Holt DP, Gobburu JVS, Peloquin CA, Mathews WB, Dannals RF, Pardo CA, Kannan S, Ivaturi VD, Jain SK, Noninvasive 11C-rifampin positron emission tomography reveals drug biodistribution in tuberculous meningitis. Sci. Transl. Med 10, eaau0965 (2018).
45. Ordonez AA, Wang H, Magombedze G, Ruiz-Bedoya CA, Srivastava S, Chen A, Tucker EW, Urbanowski ME, Pieterse L, Fabian Cardozo E, Lodge MA, Shah MR, Holt DP, Mathews WB, Dannals RF, Gobburu JVS, Peloquin CA, Rowe SP, Gumbo T, Ivaturi VD, Jain SK, Dynamic imaging in patients with tuberculosis reveals heterogeneous drug exposures in pulmonary lesions. Nat. Med 26, 529–534 (2020). [PubMed: 32066976]
46. DeMarco VP, Ordonez AA, Klunk M, Prideaux B, Wang H, Zhuo Z, Tonge PJ, Dannals RF, Holt DP, Lee CK, Weinstein EA, Dartois V, Dooley KE, Jain SK, Determination of [11C]rifampin pharmacokinetics within Mycobacterium tuberculosis-infected mice by using dynamic positron emission tomography bioimaging. Antimicrob. Agents Chemother 59, 5768–5774 (2015). [PubMed: 26169396]

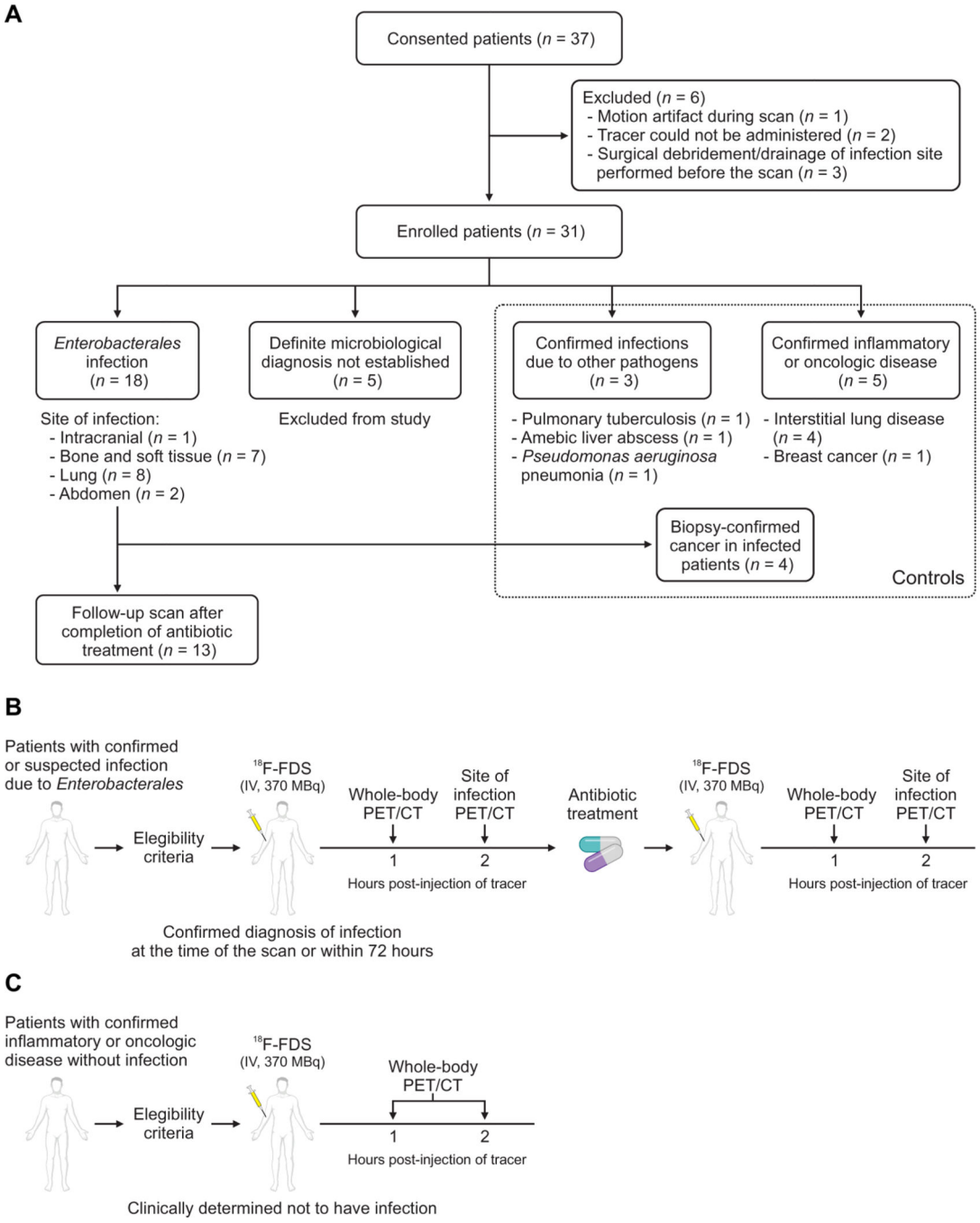

Fig. 1. Clinical study design.

(**A**) Patients with microbiologically confirmed or high suspicion for *Enterobacterales* infection and control patients with other pathologies were prospectively enrolled. For all infections, microbiological confirmation was required from the clinical/biopsy sample obtained from the infection site. Definite microbiological diagnosis was not established in five patients who were excluded from the study. Oncologic diagnosis was made via tissue biopsies, and sterile inflammatory pathologies were determined clinically and/or with tissue biopsies. Four patients with *Enterobacterales* infections had coexisting biopsy-proven

oncologic disease. Patients meeting the eligibility criteria underwent ^{18}F-FDS PET/CT at 1 and 2 hours after tracer injection. (**B**) Patients with microbiologically confirmed or high suspicion for *Enterobacterales* infection were imaged. A subset of patients with microbiologically confirmed *Enterobacterales* infection was imaged again after completion of antibiotic treatment. (**C**) Patients with confirmed inflammatory or oncologic diseases without infection were also enrolled and served as controls.

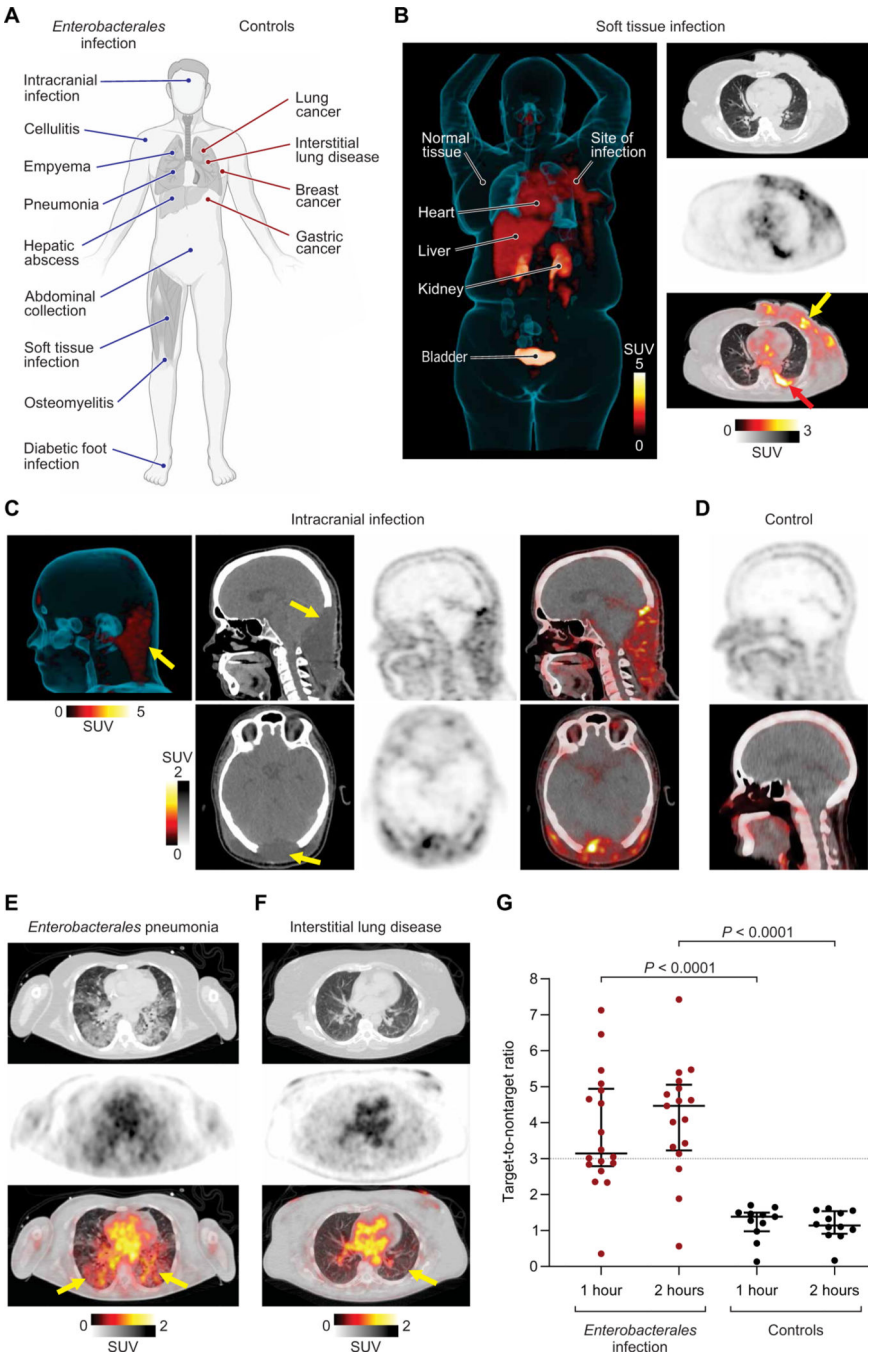

Fig. 2. ^{18}F-FDS PET can selectively detect and localize *Enterobacterales* infection at several body sites.

(**A**) Patients with microbiologically confirmed *Enterobacterales* infection (blue lines) or control patients with other pathologies (red lines) were prospectively enrolled and underwent PET/CT at 1 and 2 hours after intravenous administration of ^{18}F-FDS. (**B**) Three-dimensional (3D) maximum intensity projection (MIP), transverse CT (top right), PET (middle right), and overlaid PET/CT (bottom right) from a 67-year-old female with *Klebsiella aerogenes* cellulitis of the left breast. The breast infection site is marked by a

yellow arrow, and a microbiologically confirmed pleural effusion is also noted (red arrow). Signal is also noted in the heart (blood pool), liver, kidneys, and the urinary bladder, but no signal is noted in the brain. (**C**) From left to right, 3D MIP (left), CT, PET, and overlaid PET/CT from a sagittal view (top) and transverse view (bottom), where ^{18}F-FDS PET signal is observed in a 38-year-old male with an intracranial infection due to an MDR bacteria. ESBL-producing *K. pneumoniae* was isolated from the site of infection (yellow arrow) and cerebrospinal fluid. (**D**) Sagittal ^{18}F-FDS PET (top) and overlaid PET/CT (bottom) of the healthy brain of a control patient with low background signal. (**E**) Transverse CT (top), PET (middle), and overlaid PET/CT (bottom), where ^{18}F-FDS PET signal is observed in the infected lung areas (yellow arrows) in a 51-year-old female patient with *K. pneumoniae* pneumonia. (**F**) Transverse CT (top), PET (middle), and overlaid PET/CT (bottom) show lack of ^{18}F-FDS PET signal in the affected lung areas (yellow arrow) of a 54-year-old male with interstitial lung disease (control patient). (**G**) Target-to-nontarget ratio at 1 and 2 hours after ^{18}F-FDS injection for all 26 patients. Data are represented as median and IQR. Statistical comparisons were performed using a two-tailed Mann-Whitney *U* test. SUV, standardized uptake value.

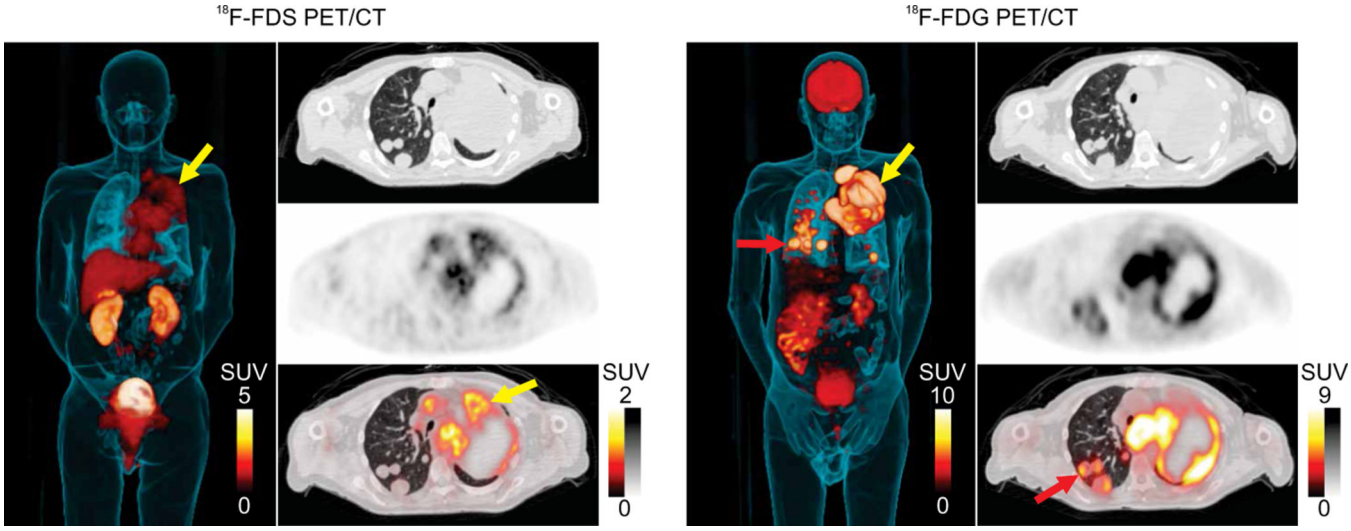

Fig. 3. Patient with *Enterobacterales* infection and coexisting biopsy-proven oncologic disease.

3D MIP, transverse CT, PET, and overlaid PET/CT are shown from a 67-year-old male with squamous cell carcinoma of the lung and *K. pneumoniae* pneumonia that underwent ^{18}F-FDG PET for clinical reasons 12 days after the study-related ^{18}F-FDS PET. ^{18}F-FDG avid pulmonary lesions are noted in red arrows; ^{18}F-FDS PET signal is noted selectively in the infected tissues in yellow arrow. ^{18}F-FDG PET signal is noted in infected lesions and in the cancerous pulmonary lesions (red arrows). Also, note the ^{18}F-FDG PET signal in the brain, which is absent for ^{18}F-FDS PET.

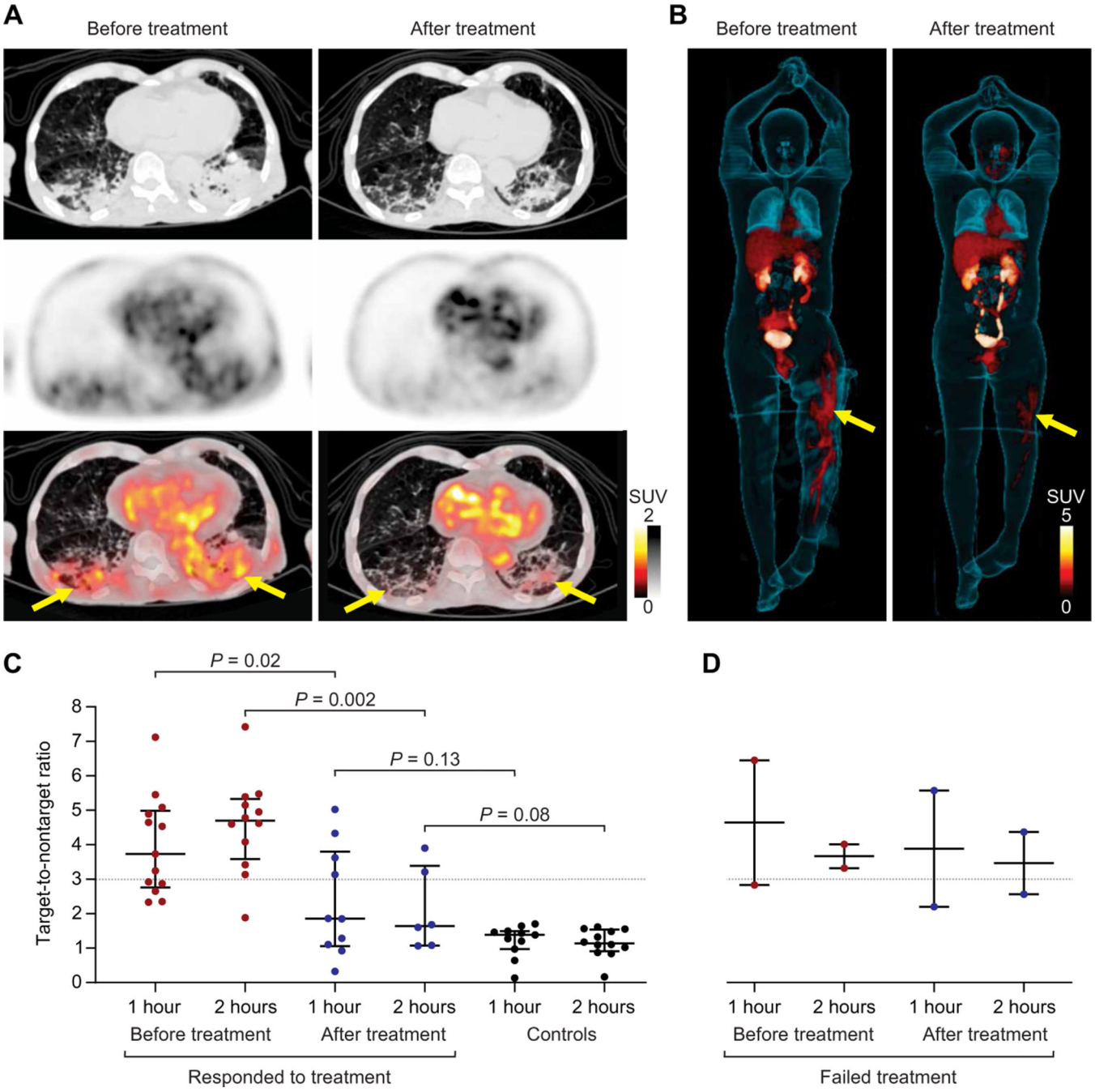

Fig. 4. ^{18}F-FDS PET can monitor antibiotic treatments.

Thirteen patients with microbiologically confirmed *Enterobacterales* infections underwent repeat ^{18}F-FDS PET/CT after completion of antibiotic treatments. Transverse CT, PET, and overlaid PET/CT from (**A**) a 91-year-old male with MDR, ESBL-producing *K. pneumoniae* pneumonia before and after appropriate treatment. The yellow arrows indicate the sites of infection. (**B**) 3D MIP from a 33-year-old male with MDR, ESBL-producing *E. coli* osteomyelitis (yellow arrows) before and after inadequate treatment. The extent of ^{18}F-FDS PET signal decreased, but the intensity did not change. (**C** and **D**) Target-to-nontarget tissue

ratio at 1 and 2 hours after ^{18}F-FDS injection for all 13 patients before and after completion of antibiotic treatments. Ratios from control patients are shown as reference. (C) Eleven patients who clinically responded to treatment and (D) two patients with treatment failure are shown. Data are represented as median and IQR. Statistical comparisons were performed using a two-tailed Mann-Whitney U test.

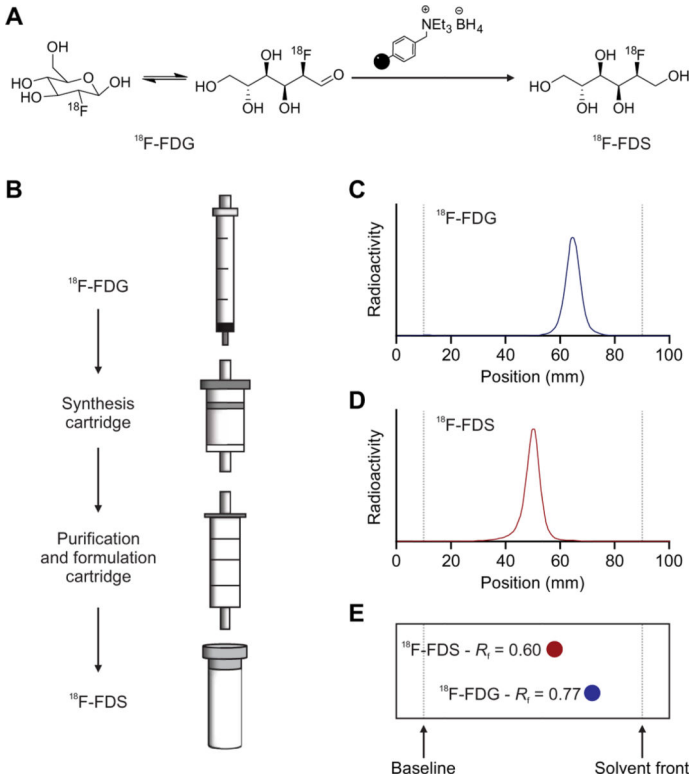

Fig. 5. Solid-phase cartridge system to synthesize ^{18}F-FDS.

(**A**) ^{18}F-FDS synthesis from ^{18}F-FDG reduction at room temperature using a solid-supported borohydride source in under 10 min. (**B**) Schematic representation of kit-based synthesis and formulation of ^{18}F-FDS, which can be achieved by eluting a solution of ^{18}F-FDG through a solid-phase synthesis cartridge followed by a purification and formulation cartridge (Chromabond Set V). Radiochemical purity (>90%, $n = 3$) was assessed by radio-TLC, which shows that ^{18}F-FDG (**C**) and ^{18}F-FDS (**D**) have different retention times and that these are identical to those of cold FDG and FDS (**E**).

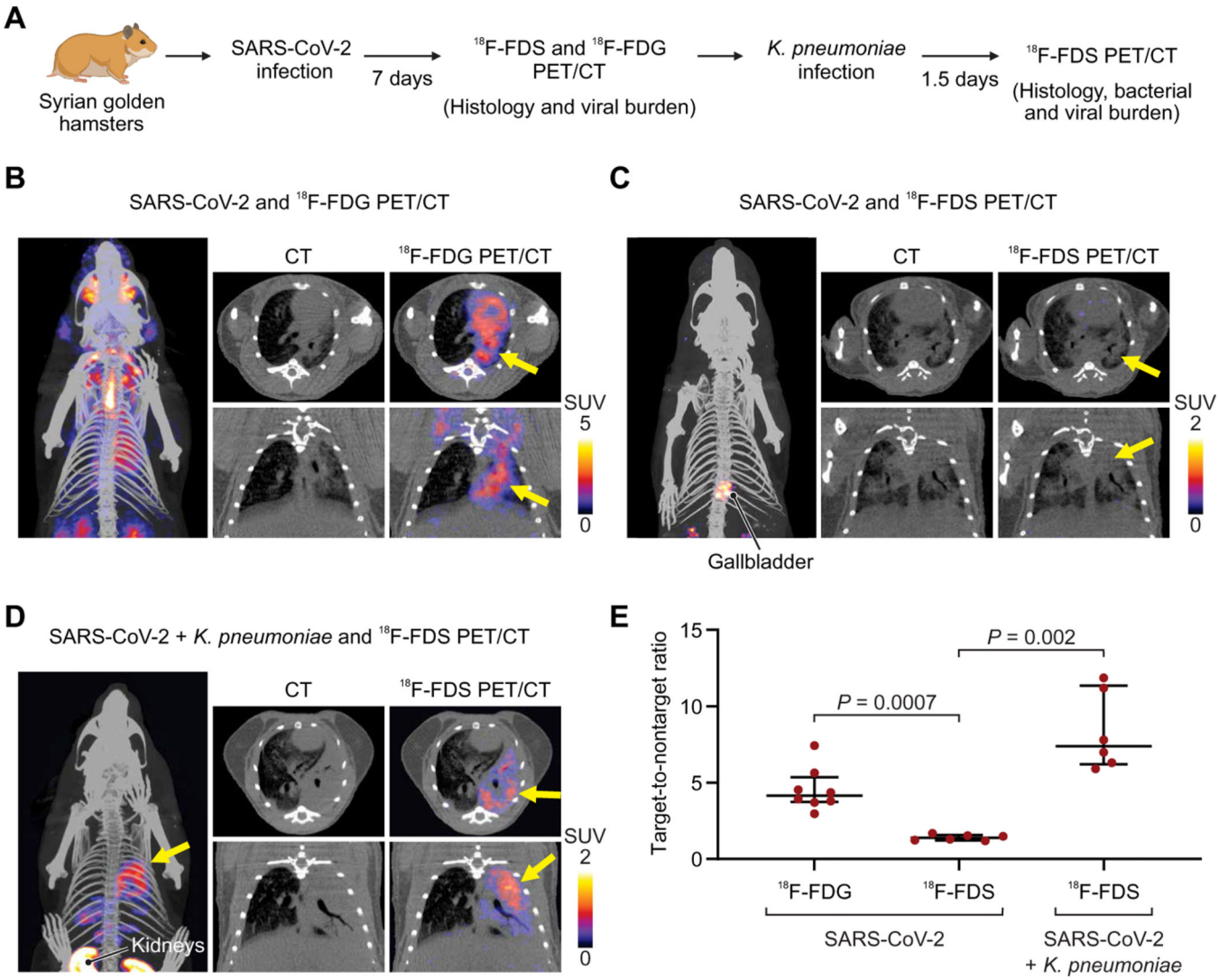

Fig. 6. ^{18}F-FDS and SARS-CoV-2 versus *K. pneumoniae* infections in hamsters.

(**A**) Syrian golden hamsters were infected intranasally with SARS-CoV-2 and, 7 days later, imaged with ^{18}F-FDS or ^{18}F-FDG PET/CT. A group of animals was euthanized at that time point for histology and quantification of viral burden (fig. S7). A subset of animals was subsequently coinfected with *K. pneumoniae* and imaged with ^{18}F-FDS PET 36 hours later. (**B**) 3D MIP, transverse (top) and coronal (bottom) CT, and overlaid PET/CT for ^{18}F-FDG in SARS-CoV-2–infected animals. The affected lung parenchyma is noted by yellow arrows. (**C**) 3D MIP, transverse (top) and coronal (bottom) CT, and overlaid PET/CT for ^{18}F-FDS in SARS-CoV-2–infected animals, where minimal signal is observed in the affected lung areas (yellow arrows). (**D**) 3D MIP, transverse (top) and coronal (bottom) CT, and overlaid PET/CT for ^{18}F-FDS in SARS-CoV-2– and *K. pneumoniae*–infected animals. Yellow arrows indicate the affected lung areas. (**E**) Target-to-nontarget ratio ^{18}F-FDS or ^{18}F-FDG injection for all animals (n = 6 animals per group of ^{18}F-FDS and n = 8 animals for ^{18}F-FDG). Data are represented as median and IQR. Statistical comparisons were performed using a two-tailed Mann-Whitney U test.